Available online at www.sciencedirect.com
ScienceDirect
Journal of the European Ceramic Society 30 (2010) 119–128
www.elsevier.com/locate/jeurceramsoc

Effect of Ar or N_2 sintering atmosphere on the high-temperature oxidation behaviour of pressureless liquid-phase-sintered α-SiC in air

F. Rodríguez-Rojas, A.L. Ortiz*, O. Borrero-López, F. Guiberteau

Departamento de Ingeniería Mecánica, Energética y de los Materiales, Escuela de Ingenierías Industriales, Universidad de Extremadura, 06071 Badajoz, Spain

Received 27 April 2009; received in revised form 28 July 2009; accepted 6 August 2009
Available online 9 September 2009

Abstract

The effect of the Ar or N_2 sintering atmosphere on the oxidation behaviour of pressureless liquid-phase-sintered (PLPS) α-SiC was studied. PLPS α-SiC specimens processed under Ar or N_2 atmospheres were isothermally oxidized at 1100–1450 °C in air for up to 500 h, and their oxidation kinetics, activation energy, and rate-controlling mechanisms were compared. It was found that, regardless of the sintering atmosphere, the oxidation is passive due to the formation of oxide scales. In addition, below 1350 °C the oxidation is protective, with a kinetics that follows initially the arctan-rate law and then the parabolic-rate law. However, from 1350 °C onwards the oxidation becomes only semi-protective, with a kinetics that obeys the arctan-rate law briefly and then the paralinear-rate law. Furthermore, the activation energies and rate-controlling mechanisms are similar for the arctan and paralinear oxidations, but different for the parabolic oxidation. It was also observed that the N_2-processed material oxidizes more slowly than the Ar-processed material below 1200 °C due to a greater crystallization of its oxide scale, whereas above 1200 °C the Ar-processed material is more oxidation-resistant due to greater viscosity of its oxide liquid. Implications concerning the optimization of the processing route of PLPS SiC for high-temperature applications in air are discussed.

Keywords: SiC; Liquid-phase sintering; Oxidation

1. Introduction

Many technological applications at high temperatures require the use of refractory ceramics that can operate safely in hostile environments, retaining sufficiently their room-temperature engineering properties. Currently, pressureless liquid-phase-sintered (PLPS) SiC is being investigated extensively as a high-temperature ceramic for structural and functional applications because it combines a very attractive set of physicochemical properties[a][1–13, and references therein] with the economy and ease of pressureless liquid-phase processing.[b] However, the moderate oxidation resistance of PLPS SiC – a non-oxide ceramic – can limit its use at high temperature in air. Thus, the challenge in this area is to develop PLPS SiC components with an adequate oxidation resistance to withstand high temperatures in oxidizing atmospheres.

Very few studies have investigated the oxidation behaviour of PLPS SiC,[14–18] and, except for the work of Liu[16] on the role of the content intergranular phase, they have not correlated sintering variables with oxidation resistance. In addition, the oxidation studies on other LPS SiCs[19–29] (*i.e.*, hot-pressed, hot-isostatic-pressed, or gas-sintered) lack a common experimental platform (*i.e.*, the starting materials, processing procedures, and oxidation conditions are very diverse), thus hindering the extraction of guidelines for the design of highly oxidation-resistant PLPS

* Corresponding author.
E-mail address: alortiz@unex.es (A.L. Ortiz).

[a] For example, as a structural material, LPS SiC is innately hard, stiff, and lightweight, moderately tough, highly refractory, very resistant to wear, creep, and thermal-shock, a good thermal conductor, and dimensionally very stable[1–10, and references therein]. As a functional material, it is a semiconductor with a wide bandgap[11–13].

[b] Firstly, pressureless sintering facilitates the fabrication of components with near-net shape without limitations on morphology and size. Secondly, the liquid-phase-assisted sintering enables dense components to be fabricated at lower temperatures and in shorter times. Since sintering of complex-shaped components can thus be performed more rapidly using ordinary high-temperature furnaces instead of hot-presses or hot-isostatic presses, there is a considerable saving in production costs.

0955-2219/$ – see front matter © 2009 Elsevier Ltd. All rights reserved.
doi:10.1016/j.jeurceramsoc.2009.08.004

SiC. Consequently, there remains a need for systematic investigations aimed at elucidating the role of the rest of the sintering variables on the oxidation behaviour of PLPS SiC.

One of the critical processing variables is the sintering atmosphere. Generally, PLPS SiC is fabricated in an atmosphere of pure Ar or N_2 to avoid oxidation during sintering. It has been demonstrated that while Ar gas is totally inert at the sintering temperatures, N_2 gas is not,[30] and approximately 1 wt% nitrogen dissolves in the liquid-stage intergranular phase making it highly refractory, viscous, and rigid which has been attributed to the replacement of twofold-coordinated oxygen by threefold-coordinated nitrogen in the crystal structure.[30] As such, the N_2 sintering atmosphere has been used to design PLPS SiC with coarsening-resistant microstructures,[30] and high internal friction,[30] sliding-wear[31] and plastic-deformation resistances,[3,32] and hardness.[33] Surprisingly, despite the beneficial effect of the N_2 sintering atmosphere on some relevant properties of PLPS SiC at room and high temperatures, its effect on oxidation resistance – a highly desirable attribute in a high-temperature non-oxide ceramic – has never before been investigated. To address this deficiency, in the present study we compare the long-term isothermal oxidation behaviour of two PLPS SiC ceramics fabricated under identical conditions with the exception of the sintering atmosphere that was either Ar or N_2. We show that the oxidation resistance of PLPS SiC is very sensitive to the sintering atmosphere, which is explained based on the corresponding oxidation mechanisms and features of the oxide scales. Implications for optimizing the processing route of PLPS SiC for high-temperature applications in air are also discussed.

2. Experimental procedure

A powder batch was prepared, containing 86.40 wt% α-SiC powder (UF-15, H.C. Starck Inc., Newton, MA, USA), 5.84 wt% Al_2O_3 (AKP-30, Sumitomo Chemical Company, New York, NY, USA), and 7.76 wt% Y_2O_3 (Fine Grade, H.C. Starck Inc., Newton, MA, USA). This batch composition is expected to yield LPS SiC ceramics with 90 vol% SiC and 10 vol% crystalline $Y_3Al_5O_{12}$ (YAG) after sintering. After successive steps of powder mixing, drying, and deagglomeration, already described in detail elsewhere,[34] the powder blend was cold-uniaxially pressed into pellets at a pressure of 50 MPa (C, Carver Inc., Wabash, IN, USA), which were subsequently cold-isostatically pressed (CP360, AIP, Columbus, OH) at a pressure of 350 MPa. The individual green pellets were first embedded in powder beds (coarse SiC plus Al_2O_3 powders) inside graphite crucibles with screwable lids to avoid mass loss during sintering, and were then pressureless sintered (1000-3560-FP20, Thermal Technology Inc., Santa Rosa, CA, USA) under the following conditions: peak temperature of 1950 °C, heating and cooling rates of 600 and 1200 °C/h, respectively, hold time at peak temperature of 1 h, and flowing atmosphere of Ar or N_2 gas. The resulting ceramics, which will be referred to as PLPS SiC–Ar and PLPS SiC–N_2, were cleaned and surface layers were ground off. The density of the as-processed materials was measured using Archimedes' method with distilled water as the immersion medium, and their microstructure, residual porosity and phase composition were examined by scanning electron microscopy (SEM; S-3600N, Hitachi, Japan) and X-ray diffractometry (XRD; PW-1800, Philips Research Laboratory, Eindhoven, The Netherlands), respectively. The XRD patterns were obtained using Cu-Kα incident radiation and a graphite secondary monochromator, whereas the SEM observations were made with secondary electrons on cross sections (polished to 1-μm finish). The nitrogen content in PLPS SiC–N_2 was measured using the inert gas (helium) fusion (IGF) method (TNT-414, Leco Corporation, St. Joseph, MI).

As conventionally done in non-oxide advanced ceramics, long-term isothermal oxidation behaviour of PLPS SiC–Ar and PLPS SiC–N_2 was evaluated by furnace oxidation. To this end, cubes 1 cm × 1 cm × 1 cm were cut out from the two as-processed materials, and all cube faces were diamond-polished to a 1-μm finish. Oxidation tests were performed in a bottom-loading furnace (Interbil, Spain) carefully cleaned to prevent from contamination, under the following conditions: atmosphere of ambient air, temperatures in the interval 1100–1450 °C, and exposure times in the range 0–500 h, with the PLPS SiCs resting on high-purity CVD SiC plates to avoid contact with the furnace parts. The long-term oxidation curves were constructed by repeating successive steps of removing the cubes from the furnace at predesigned time intervals to be cold-weighed to ±0.0001 g and then returning them to the furnace for further oxidation, until a maximum oxidizing time of 500 h was reached. To preclude a zero-point shift in the oxidation curves, the furnace was heated empty up to oxidizing temperature and then the PLPS SiCs were placed in its interior.

Similarly to the as-processed materials, the oxidized materials were also characterized by XRD and SEM, plus SEM examinations on plane views (without additional preparation) and X-ray energy dispersive spectrometry (XEDS; XFLASH Detector 3001, Röntec GmbH, Germany) analysis. The XEDS spectra were interpreted using the *ZAF*-factor technique for elemental chemical analysis.[35]

3. Results

3.1. Microstructure of the as-processed samples

Fig. 1 shows representative SEM images of the microstructures of PLPS SiC–Ar and PLPS SiC–N_2 in the as-processed condition. It can be seen that the two ceramics are fully dense as there are no pores, which is consistent with the densities that were measured by Archimedes' method that indicated complete densification. In addition, it can also be observed that the two ceramics have nominally the same microstructure. In particular, in both cases the average size and aspect ratio of the SiC grains (dark phase) determined by image analysis are ∼0.6 μm and 1.4, respectively, and the grains are embedded in an oxide intergranular phase (bright phase). The major difference between the two materials is that PLPS SiC–N_2 contains ∼0.5 wt% nitrogen, which has been incorporated from the N_2 sintering atmosphere. Note that, although IGF does not provide information on the

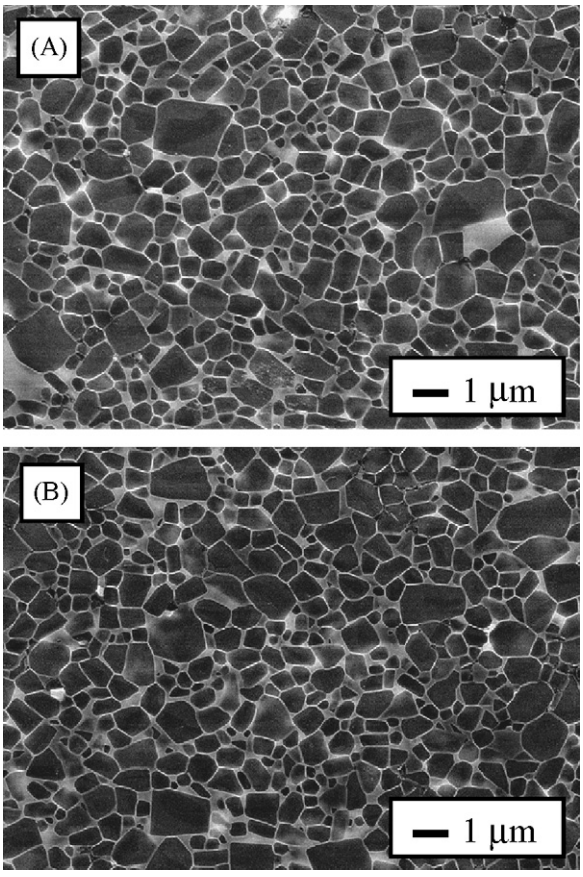

Fig. 1. SEM micrographs of polished and plasma-etched microstructures of PLPS SiC processed using sintering atmospheres of (A) Ar and (B) N_2.

location of the dissolved nitrogen, internal friction measurements performed on other PLPS SiCs have demonstrated that it resides mostly in the intergranular phase.[30] Thus, the intergranular phase in PLPS SiC–N_2 is YAG with nitrogen in solid solution.

Shown in Fig. 2 are the XRD patterns of the as-processed PLPS SiC–Ar and PLPS SiC–N_2. It can be seen that the two

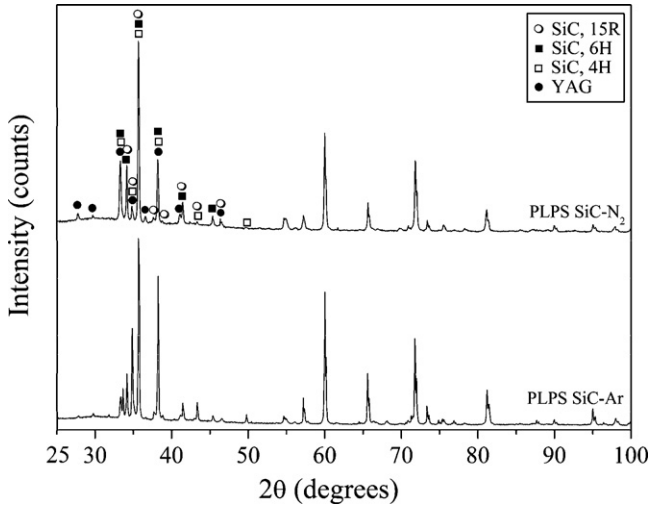

Fig. 2. XRD patterns of PLPS SiC processed using sintering atmospheres of Ar and N_2. The phase identification is shown only up to about 50° 2θ.

ceramics are only composed of various α-SiC polytypes (*i.e.*, 4H, 6H, and 15R) and of YAG. Nevertheless, two differences can be deduced from the XRD patterns. First, PLPS SiC–Ar contains a greater proportion of 4H, less of 6H, and similar of 15R than PLPS SiC–N_2. This result can be explained considering that the α-SiC starting powders are composed of 87 wt% 6H and 13 wt% 15R, and that the N_2 sintering atmosphere inhibits the phase transformations between polytypes[30] while the Ar-sintering atmosphere promotes the 6H → 4H transformation.[36,37] Second, the nitrogen solutes have introduced structural defects into the lattice of the YAG crystals because their peaks in PLPS SiC–N_2 exhibit additional Gaussian broadening with respect to PLPS SiC–Ar, and the XRD theory establishes that lattice defects introduce Gaussian broadening whereas the nanocrystallites induce Lorentzian broadening.[38]

3.2. Oxidation kinetics

Compared in Fig. 3 are the specific mass-change curves for PLPS SiC–Ar and PLPS SiC–N_2 isothermally oxidized in air at 1100–1450 °C. As can be seen, there exist appreciable

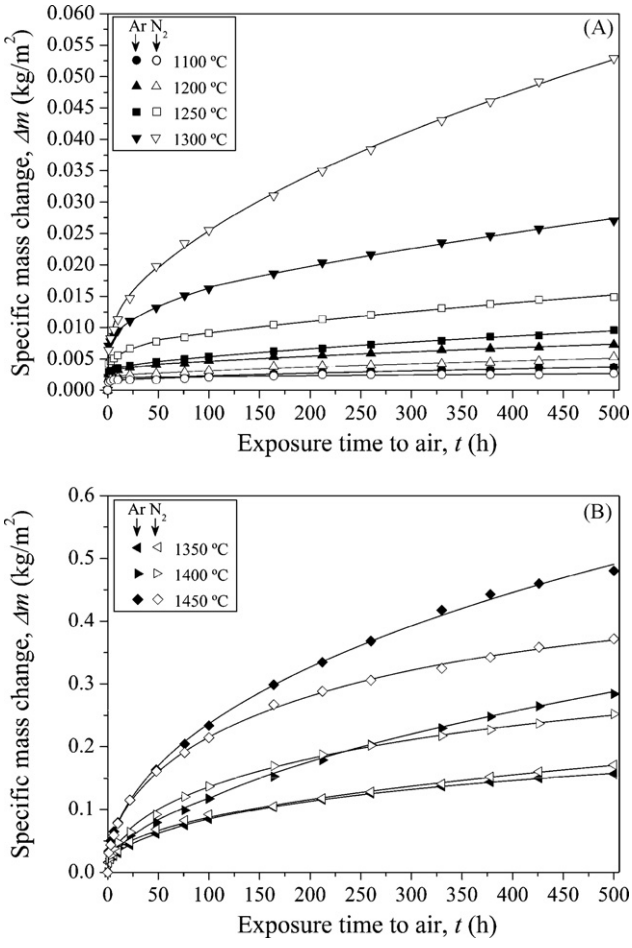

Fig. 3. Oxidation curves of PLPS SiC in air at temperatures in the intervals (A) 1100–1300 °C and (B) 1350–1450 °C. The points are the experimental data (closed symbols for PLPS SiC–Ar and open symbols for PLPS SiC–N_2). The solid lines are generated by combining two oxidation kinetics models (discussed in the text).

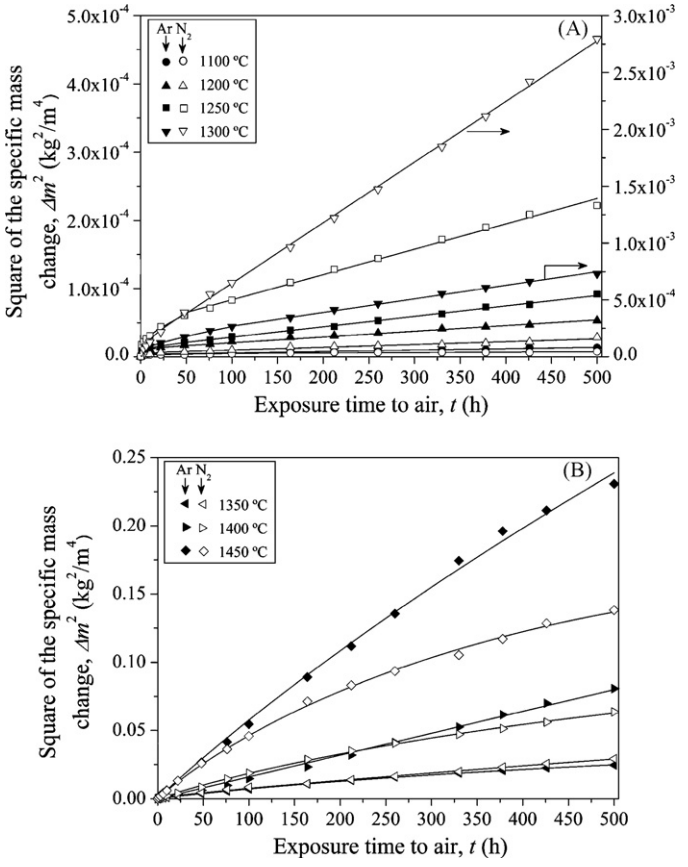

Fig. 4. Square of the oxidation curves of PLPS SiC–Ar and PLPS SiC–N_2 in air at temperatures in the intervals (A) 1100–1300 °C and (B) 1350–1450 °C. The points are the experimental data (closed symbols for PLPS SiC–Ar and open symbols for PLPS SiC–N_2). The solid lines are generated by combining two oxidation kinetics models (discussed in the text).

differences between the oxidation kinetics of the two materials. Nevertheless, mass gain is always observed, indicating that the oxidation is in all cases passive because active oxidation is accompanied by mass loss.[39] Furthermore, the oxidation kinetics is curved, revealing that the long-term oxidation is not controlled by the speed of an interface reaction which would lead to linear oxidation kinetics.[39] It thus follows that the passive oxidation of the two ceramics has to be controlled necessarily by diffusion alone, or by the competition between diffusion and an interface reaction.

To identify the nature of the oxidation of the two materials, the oxidation data are plotted as $(\Delta m_s)^2$-versus-t charts in Fig. 4. It can be observed that the $(\Delta m_s)^2$–t relationship is not linear over the entire t range, indicating that the oxidation kinetics in Fig. 3 does not obey completely the typical parabolic-rate law of materials with constant diffusion cross-sectional area.[c] Instead, the $(\Delta m_s)^2$–t relationships are first concave with respect to the t axis and then linear (called Type I oxidation curves hereafter) below 1350 °C, or slightly non-linear (called Type II oxidation curves hereafter) from 1350 °C onwards. In addition, it is also noted that the duration of the concave stretch decreases from various tens of hours to only a few hours as the oxidizing temperature increases. These types of passive oxidation behaviour in two regimes are characteristic of non-oxide ceramics in which the oxide scale crystallizes progressively during oxidation,[39–44] and indicate that a combination of kinetics models is needed to explain the oxidation curves. Briefly, it is well established that if oxide scale devitrifies gradually during the first moments of the oxidation, then the effective diffusion rate is time-dependent due to the progressive reduction in the amorphous cross section available for diffusion because the crystalline precipitates act as a barrier against diffusion.[39] In this scenario, the oxidation kinetics will initially obey an arctan-rate law of the form[39–44]:

$$\Delta m_s = \frac{\beta\sqrt{k_p}(1-f)}{\sqrt[3]{(\beta - 1/t_0)^2}} \arctan\sqrt{(\beta - 1/t_0)t} + \frac{\sqrt{k_p}(\beta f - 1/t_0)}{\beta - 1/t_0}\sqrt{t} + b \quad (1)$$

where Δm_s is the specific mass variation (weight change per surface area), k_p the parabolic-rate constant, β the rate constant for the decrease of the area, f the fraction of original area that still remains amorphous, t_0 the time at which the crystallization process stops, and b an additive constant (ideally equal to zero) that accounts for the possible mass change at the beginning of the isothermal oxidation test ($t = 0$). At t_0 the oxidation kinetics changes, and is no longer given by the arctan-rate law because the cross section available for diffusion, although reduced, becomes constant and consequently so does the effective diffusion rate. In particular, if the oxide scale is protective, then the oxidation kinetics after t_0 will satisfy a parabolic-rate law of the form[39]:

$$\Delta m_s = \sqrt{k_p^0 t + b_0} \quad (2)$$

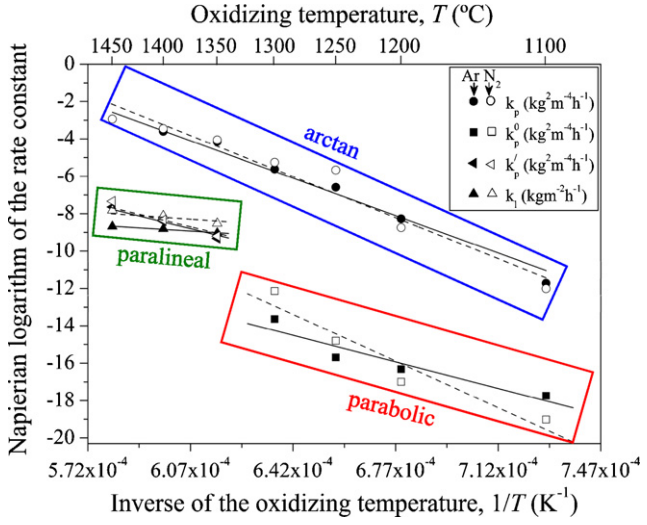

Fig. 5. The Arrhenius plot of the rate constants for the arctan, parabolic, and paralinear oxidations of PLPS SiC–Ar and PLPS SiC–N_2 in air in the temperature range 1100–1450 °C. The solid lines are linear fits to the point data (closed symbols for PLPS SiC–Ar and open symbols for PLPS SiC–N_2). For clarity, the different regimes are indicated with boxes.

[c] This conclusion was corroborated also using $(\Delta m_s)^2/t$-versus-t or Δm_s-versus-$t^{0.5}$ charts.

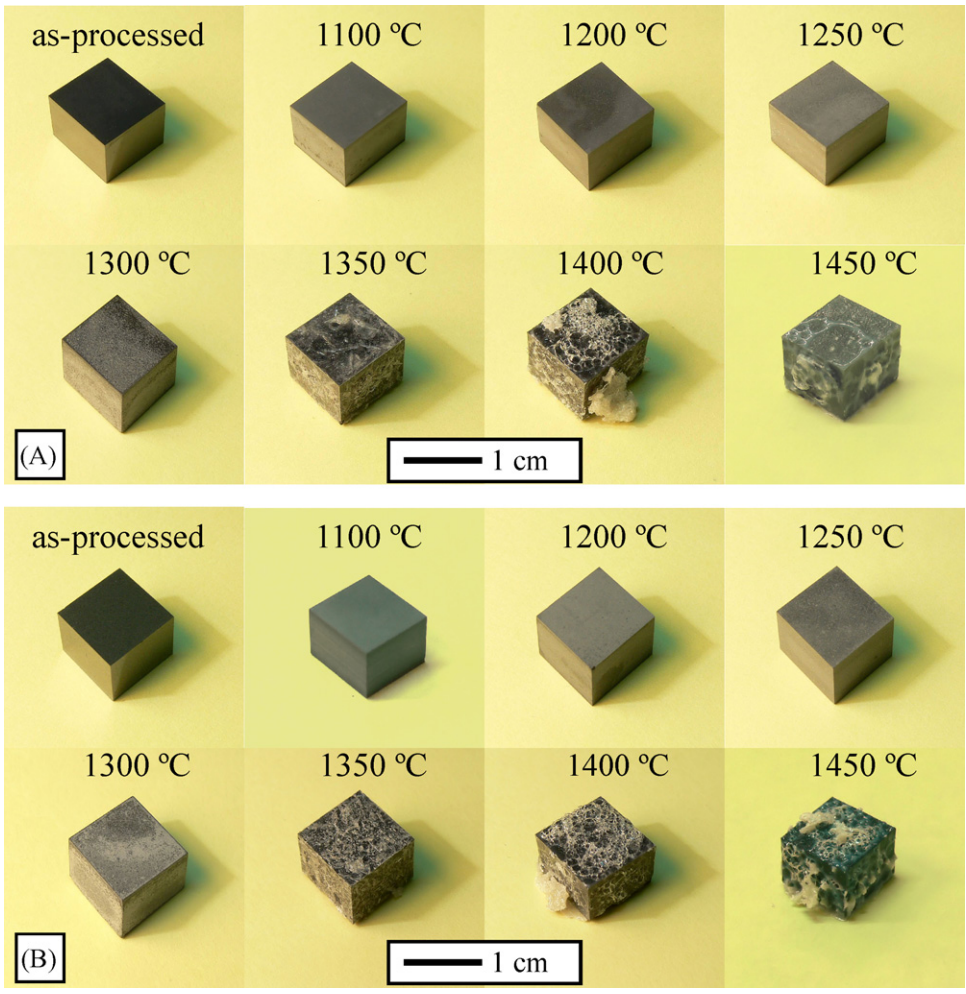

Fig. 6. Macrographs of (A) PLPS SiC–Ar and (B) PLPS SiC–N_2 before and after oxidation in air for 500 h at temperatures in the interval 1100–1450 °C.

where k_p^0 is the parabolic-rate constant and b_0 is related to the mass change before t_0. However, if the oxide scale is only semi-protective because it simultaneously grows and recesses, then the oxidation kinetics after t_0 will follow a paralinear-rate law of the form[28,39]:

$$\Delta m_s = \sqrt{k_p' t} - k_l t + b_0' \quad (3)$$

where k_p' and k_l are the parabolic and linear rate constants, respectively, and b_0' has the same meaning as b_0.

It follows from the above discussion that Type I and II oxidation curves both satisfy first the arctan-rate law, although then Type I curves obey the parabolic-rate law whereas Type II curves obey the paralinear-rate law. Included in Fig. 3 are the model curves obtained by nonlinear least-squares fitting the combination of the arctan plus parabolic-rate laws to Type I oxidation curves and the combination of the arctan plus paralinear laws to Type II oxidation curves. It can be seen that the fits captured the oxidation kinetics remarkably well, hence supporting the validity of the proposed combinations of rate laws. Indeed, the intents to model the oxidation kinetics with the rest of the simple rate laws or their possible combinations[d] did not lead any to satisfactory fits. The rate constants determined by curve modelling for the arctan (k_p), parabolic (k_p^0), and paralinear oxidation (k_p' and k_l) regimes are shown in the Arrhenius-type plots of Fig. 5.

The activation energies (Q) for the oxidation of PLPS SiC–Ar and PLPS SiC–N_2 can be then determined by fitting the Arrhenius equation[39]:

$$\ln k = \ln k^* - \frac{Q}{RT} \quad (4)$$

to the rate constants k_p, k_p^0, k_p', and k_l in Fig. 5, where k^* is the pre-exponential factor, R the universal gas constant (8.314 J/mol K), and T the absolute temperature. The best fits lines are included in Fig. 5, from which the following activation energies are obtained, respectively, for the oxidation of PLPS SiC–Ar and PLPS SiC–N_2: (i) in the arctan regime, 504 ± 32 and 521 ± 48 kJ/mol; (ii) in the parabolic regime, 310 ± 47 and 593 ± 68 kJ/mol; and (iii) in the paralinear regime, 320 ± 14 and 315 ± 12 kJ/mol for

[d] That is, the arctan, parabolic, and paralinear laws, as well as the parabolic + arctan, parabolic + paralinear, paralinear + parabolic, and paralinear + arctan laws, plus the arctan + paralinear laws for Type I oxidation curves and the arctan + parabolic laws for Type II oxidation curves.

the growth of the oxide scale, and 90 ± 10 and 81 ± 12 kJ/mol for its recession.

3.3. Microstructure of the oxidized samples

Shown in Fig. 6 are low-magnification macrographs of PLPS SiC–Ar and PLPS SiC–N_2 before and after oxidation in air for 500 h. As can be observed, the oxidized samples exhibit oxide scales on their surfaces, which is the sole condition required for the oxidation to be classified as passive.[39] The presence of oxide scales was further confirmed by SEM observation of cross sections (not shown). It is also observed in Fig. 6 that the sample surface starts degrading dramatically at 1350 °C. Unlike the samples oxidized at lower temperatures, whose oxide scale is flat, smooth, and compact, the oxide scale of the samples oxidized from 1350 °C onwards is blistered and rough, and has melted and flowed out partially, indicating that the long-term oxidation is paralinear at these temperatures due to the concurrence of mass gain and loss processes. This is entirely consistent with the modelling of the oxidation kinetics.

Shown in Fig. 7 are representative plane-view SEM images of PLPS SiC–Ar and PLPS SiC–N_2 oxidized in air at 1200 °C for 500 h. As can be observed in Fig. 7A, the oxide scale of

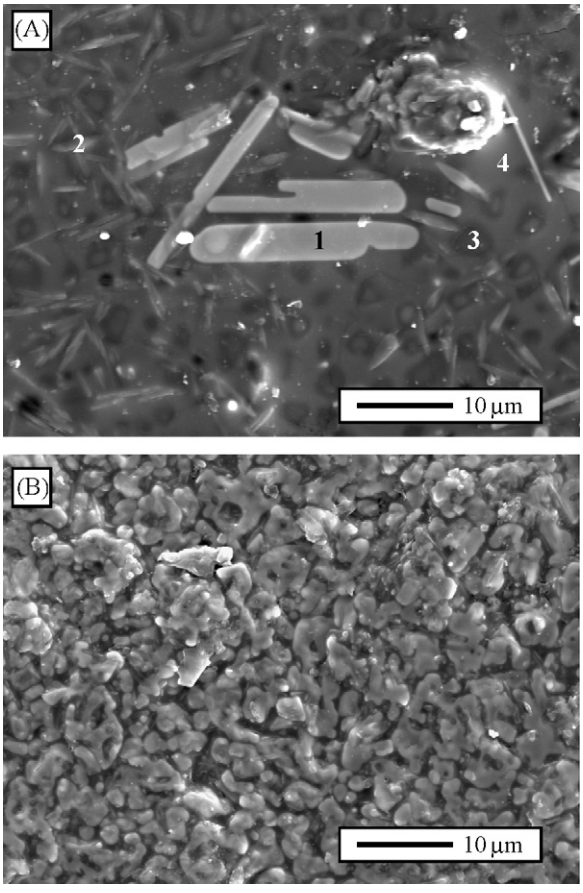

Fig. 7. SEM micrograph of the surface of (A) PLPS SiC–Ar and (B) PLPS SiC–N_2 after oxidation in air at 1200 °C for 500 h. The regions marked with 1, 2, 3, and 4 in (A) correspond to the $Y_2Si_2O_7$ crystals, $Al_2Si_2O_7$ crystals, SiO_2 grains, and vitreous matrix, respectively.

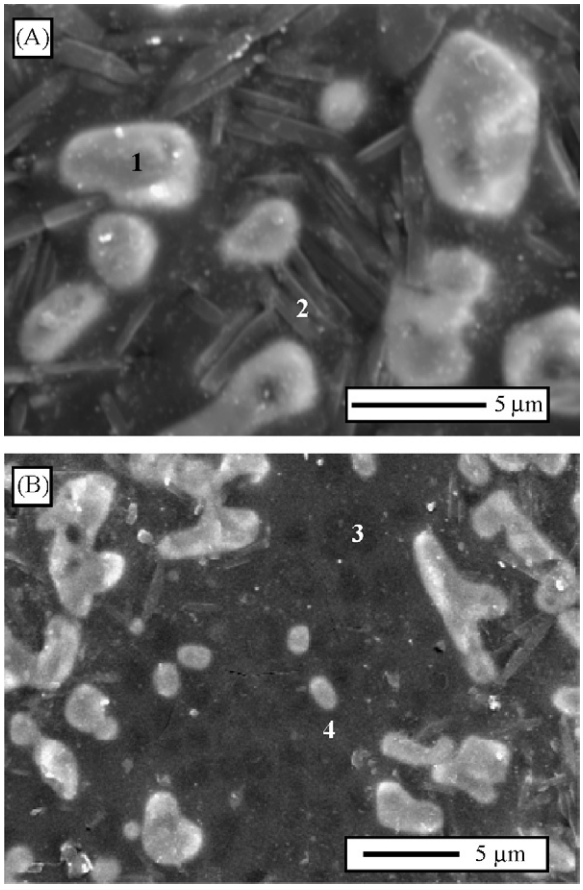

Fig. 8. SEM micrograph of the subsurface region of PLPS SiC–N_2 after oxidation in air at 1200 °C for 500 h. To explore the inner oxide scale, the outermost layer of $Y_2Si_2O_7$ crystals has been removed. The regions marked with 1, 2, 3, and 4 in (A) and (B) correspond to the $Y_2Si_2O_7$ crystals, $Al_2Si_2O_7$ crystals, SiO_2 grains, and vitreous matrix, respectively.

PLPS SiC–Ar consists of a mixture of two types of crystals and equiaxed grains embedded in a matrix that seems to be vitreous. The XEDS analysis indicated that the crystals have the $Al_2Si_2O_7$ and $Y_2Si_2O_7$ stoichiometries, respectively, that the equiaxed grains are SiO_2, and that the matrix contains various aluminium silicates and complex yttrium aluminium silicates or yttrium silicates in smaller amounts. These stoichiometries have been confirmed by XRD, as will be shown later. However, as can be seen in Fig. 7B the oxide scale in PLPS SiC–N_2 contains apparently only one type of crystals, identified as $Y_2Si_2O_7$ by XEDS. Nevertheless, as shown in the SEM images of Fig. 8, beneath the $Y_2Si_2O_7$ layer there is another layer that contains $Al_2Si_2O_7$ crystals, SiO_2 grains, and the Al–Si–Y–O matrix. Thus, compared to PLPS SiC–Ar the feature of interest is that the oxide scale of PLPS SiC–N_2 has a two-layered structure whose top $Y_2Si_2O_7$ layer is markedly crystalline and covers almost completely the sample surface.

Shown in Fig. 9 are representative plane-view SEM images of PLPS SiC–Ar and PLPS SiC–N_2 oxidized in air at 1350 °C for 500 h. As can be observed, the two oxide scales contain some large crystals, identified as $Y_2Si_2O_7$ by XEDS, and glassy phases. Nevertheless, the important difference is that the oxide scale in PLPS SiC–N_2 has a much more glassy appearance. In

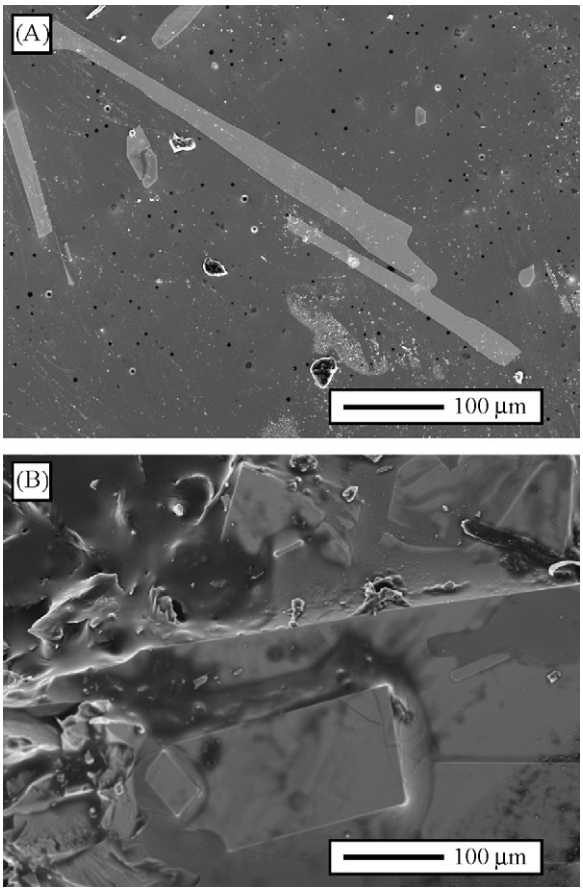

Fig. 9. SEM micrograph of the surface of (A) PLPS SiC–Ar and (B) PLPS SiC–N_2 after oxidation in air at 1350 °C for 500 h.

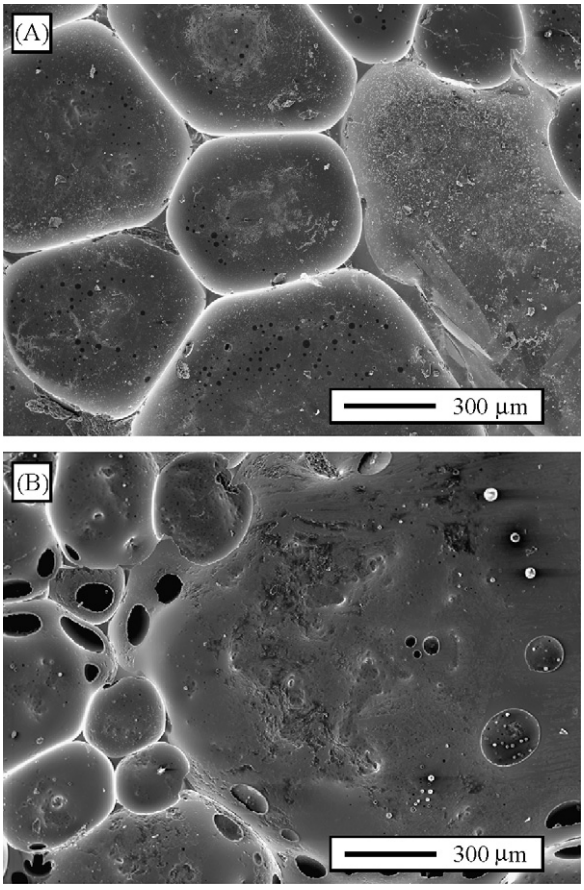

Fig. 10. SEM micrograph of the surface of (A) PLPS SiC–Ar and (B) PLPS SiC–N_2 after oxidation in air at 1400 °C for 500 h.

addition, the XEDS analysis revealed that the glassy phase in PLPS SiC–N_2 was richer in Y and Al.

Fig. 10 shows representative plane-view SEM images of PLPS SiC–Ar and PLPS SiC–N_2 oxidized in air at 1400 °C for 500 h. As can be seen, the two oxide scales exhibit a coarse drop-like structure that is likely to have originated from the solidification of a liquid, and also contain some pores that are likely the bubbles created by gaseous oxidation products. Nevertheless, the oxide scale in PLPS SiC–N_2 is clearly more degraded, revealing that the liquid formed had lower high-temperature viscosity.

Shown in Fig. 11 are the XRD patterns of PLPS SiC–Ar and PLPS SiC–N_2 after oxidation in air at 1200, 1350, and 1400 °C for 500 h, from which several distinct features can be noted. Firstly, compared to the as-processed conditions (see Fig. 2), there are extra peaks attributable to the oxidation products already detected by XEDS, whose intensity decreases substantially at 1350 °C and above. Secondly, the intensity of the SiC peaks decreases continuously as the oxidizing temperature increases, becoming hardly visible from 1350 °C onwards. Thirdly, a few peaks from the $Y_2Si_2O_7$ phase become strongly favoured over the rest at 1350 °C. And finally, the background level increases with increasing oxidizing temperature, and in particular from 1350 °C onwards. From these observations it can be concluded that: (i) the oxidation is passive as condensed phases (crystalline and amorphous) formed on the sample surfaces, (ii) the thickness of the oxide scale increases with increasing oxidation temperature, (iii) the $Y_2Si_2O_7$ exhibits texture at 1350 °C, and (iv) the oxide scales becomes almost completely glassy from 1350 °C onwards. These conclusions are in excellent agreement with those from modelling the oxidation kinetics and the SEM analysis.

The comparison between the XRD patterns of PLPS SiC–Ar and PLPS SiC–N_2 is also very interesting. It can be observed that at 1200 °C the intensity of the oxidation product peaks is higher and the background lower in PLPS SiC–N_2, indicating that its oxide scale is more crystalline. This is consistent with the SEM observations of Fig. 7. At 1350 °C it is noted that the background level is lower and the intensity of the oxidation products peaks higher in PLPS SiC–Ar, revealing that its scale is more crystalline. This is consistent with the SEM observations of Fig. 9. Finally, at 1400 °C the two XRD patterns are very similar, although the background level is lower and the intensity of the SiC peaks higher in PLPS SiC–N_2, thus indicating that its oxide scale is thinner.

4. Discussion

The results presented above reveal that the choice of the sintering atmosphere (Ar or N_2) has significant practical impli-

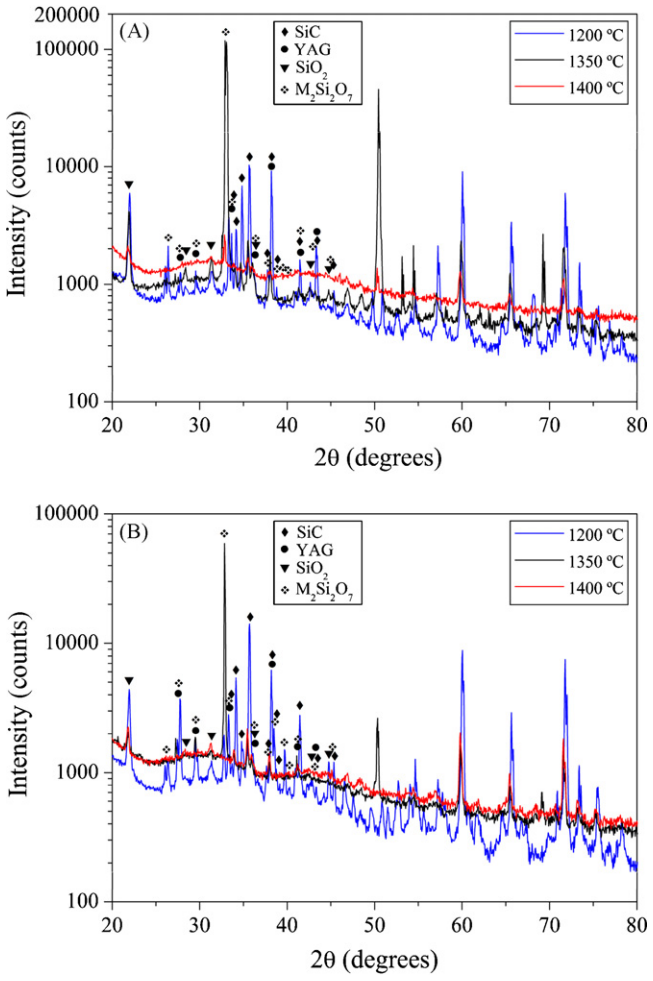

Fig. 11. XRD patterns of (A) PLPS SiC–Ar and (B) PLPS SiC–N_2 after oxidation in air at 1200, 1350, and 1400 °C for 500 h. The phase identification is shown only up to about 45° 2θ, whereas the patterns are plotted up to 80° 2θ to observe the background more easily. M is Y and/or Al. The diffracted intensities are plotted in logarithmic scale to facilitate the observation of the weakest peaks.

cations for the design of oxidation-resistant PLPS SiC. In particular, it can be concluded from the rate constants (Fig. 5) determined for the arctan (k_p), parabolic (k_p^0), and paralinear oxidation (k_p' and k_l) regimes that: (i) PLPS SiC–N_2 is more oxidation-resistant than PLPS SiC–Ar up to 1200 °C because k_p and especially k_p^0 are both lower; (ii) from 1200 °C onwards the previous trend changes, and PLPS SiC–N_2 becomes less oxidation-resistant as up to 1350 °C k_p and especially k_p^0 are now both greater and at 1350 °C and above PLPS SiC–N_2 loses mass faster than PLPS SiC–Ar because k_l is always greater. It should be mentioned that the trends described below 1350 °C can also be deduced from the mere observation of the oxidation curves in Fig. 3 because these oxidations are arctan + parabolic and therefore the specific mass gain correlates inversely with the oxidation resistance; however, this correlation breaks down for the arctan + paralinear oxidation due to the concurrence of gain and loss of specific mass, and thus the trends described from 1350 °C onwards cannot be reached from the simple examination of Fig. 3, but require necessarily the determination of the oxidation-rate constants k_p' and k_l as has been done here.

The sintering atmosphere, on the contrary, does not affect the nature of the oxidation of PLPS SiC, which is always passive at temperatures in the range 1100–1450 °C due to the formation of oxide scales. These oxide scales are protective below 1350 °C because the oxidation is arctan + paralinear, and only semi-protective from there onwards because the oxidation is arctan + paralinear. With respect to the oxidation mechanisms, the SEM, XEDS, and XRD analyses suggest that the oxidation reactions are the same in both cases. Specifically, SiC would react first with O_2 via the following reaction:

$$2SiC(s) + 3O_2(g) \rightarrow 2SiO_2(s) + 2CO(g) \quad (I)$$

Then, part of the SiO_2 formed from reaction (I) would react with YAG ($Y_3Al_5O_{12}$) to form $Al_2Si_2O_7$ and $Y_2Si_2O_7$ according to the following reaction:

$$16SiO_2(s) + 2Y_3Al_5O_{12}(s) \rightarrow 5Al_2Si_2O_7(s) + 3Y_2Si_2O_7(s) \quad (II)$$

The formation of these silicates results in a zone depleted of Y^{3+} and Al^{3+} cations immediately below the oxide scale. The compositional gradient of Y^{3+} and Al^{3+} between the oxide scale and the unoxidized material thus induces the migration of these cations to their interface. It is well established that these cations favour further the crystallization of the oxide scale while reducing the viscosity of the silicate liquid.[39,40,45] Since the crystallization slows down the oxidation kinetics and the reduced viscosity speeds it up, the overall diffusivity will thus be determined by the resulting balance of these opposing tendencies. At the high oxidizing temperature, pores can be formed in the oxide scales due to the gaseous products generated by the carbothermal reduction of the YAG intergranular phase through the following reaction:

$$Y_3Al_5O_{12}(s) + 4CO(g) \rightarrow 3YAlO_3(s) + Al_2OC(g) + 3CO_2(g) \quad (III)$$

where the CO(g) reactant is a product of reaction (I). The absence of its peaks in the XRD patterns indicates that $YAlO_3$ is in amorphous state.

The oxidation behaviours of PLPS SiC–Ar and PLPS SiC–N_2 are also similar in the sense that both are characterized by two distinct stages at all temperatures: (i) initial arctan oxidation, followed by (ii) parabolic oxidation below 1350 °C, or paralinear oxidation from there onwards. Therefore, the principal distinction between their oxidation behaviours is in the rate-controlling mechanism of the parabolic oxidation regime, as concluded from the Arrhenius plots in Fig. 5. First, the activation energies of the arctan oxidation are similar and as high as 504 ± 32 kJ/mol for PLPS SiC–Ar and 521 ± 48 kJ/mol for PLPS SiC–N_2, indicating that the rate-controlling mechanism is in both cases outward diffusion of Y^{3+} and Al^{3+} cations from the intergranular phase into the oxide scale.[21,22] Second, the activation energy of the parabolic oxidation is about two times higher in PLPS SiC–N_2 than in PLPS SiC–Ar (593 ± 68 kJ/mol versus 310 ± 47 kJ/mol, respectively), revealing a difference in the rate-controlling mechanism. The moderate value of the

activation energy in the former is ascribed to inward diffusion of oxygen through the oxide scale,[39] while again the much higher activation energy in the latter is ascribed to outward diffusion of metal cations from the intergranular phase into the oxide scale. Third, the activation energies for the growth and recession of the oxide scale in the paralinear oxidation are very similar (320 ± 14 and 90 ± 10 kJ/mol for PLPS SiC–Ar versus 315 ± 12 and 81 ± 12 kJ/mol for PLPS SiC–N_2). Therefore, it is proposed that in both cases the oxide scales grow controlled by inward diffusion of oxygen, and recess controlled by viscous flow and escape of gases.

Let us consider now the effect of the Ar or N_2 sintering atmosphere on the oxidation resistance of PLPS SiC. As demonstrated in this study, PLPS SiC–N_2 oxidizes more slowly than PLPS SiC–Ar below 1200 °C. Considering the SEM (Figs. 7 and 8) and XRD (Fig. 11) analyses, this is attributed to the greater crystallinity of its oxide scale at these temperatures, since the diffusion rate through crystalline phases is various orders of magnitude slower than through amorphous phases.[39] The origin for the greater crystallinity in PLPS SiC–N_2 is not totally clear, and requires further investigation in the future. At this stage, the most likely explanation is that the structural defects in the YAG lattice produced by the nitrogen solutes make it more reactive because defects can raise its free energy or destabilize it, thus speeding up the formation of the protective crystalline oxides.

On the contrary, above 1200 °C PLPS SiC–N_2 becomes less oxidation-resistant than PLPS SiC–Ar. As revealed by the SEM (Figs. 9 and 10) and XRD (Fig. 11) analyses, this is attributed to the lower viscosity of its oxide liquid, and the attendant various orders of magnitude increase in the diffusion rate.[38,44] In turn, such a reduction in the viscosity is due to a combination of the poorer crystallinity,[39,45] the higher Y^{3+} and Al^{3+} content in the glassy phase,[39,45] and the lower eutectic temperature in the presence of nitrogen (1282 °C in the system Y–Si–Al–O–N versus 1371 °C in the system Y–Si–Al–O).[46,47]

5. Conclusions

The effect of the sintering atmosphere (Ar or N_2) on the long-term oxidation behaviour of PLPS SiC in air was investigated in the temperature range 1100–1450 °C. Based on this study, the following conclusions can be drawn:

(1) Regardless of the sintering atmosphere, the oxidation of PLPS SiC at these temperatures is passive and has a two-stage kinetics that first obeys the arctan-rate law and then the parabolic-rate law below 1350 °C or the paralinear-rate law from there onwards. This complex oxidation kinetics reflects the initial crystallization of the oxide scales, and their protective character below 1350 °C but only semi-protective at and above 1350 °C.

(2) The sintering atmosphere does not affect the activation energy for the arctan and paralinear oxidation regimes, which are controlled by outward diffusion of Y^{3+} and Al^{3+} cations and by the competition between inward diffusion of oxygen and viscous flow/escape of gases, respectively. However, the sintering atmosphere does influence the activation energy for the parabolic oxidation regime, which is controlled by inward diffusion of oxygen in the Ar-processed material and by outward diffusion of Y^{3+} and Al^{3+} cations in the N_2-processed material.

(3) The sintering atmosphere conditions the oxidation resistance of PLPS SiC. Thus, the N_2-processed material is more oxidation-resistant up to 1200 °C, which is due to the greater crystallization of its oxide scale at these moderate temperatures. In contrast, above 1200 °C the Ar-processed material becomes more oxidation-resistant, which is due to the greater viscosity of its oxide scale.

(4) The sintering atmosphere is another approach to tailoring the oxidation resistance in PLPS SiC ceramics.

Acknowledgment

This work was supported by the Ministerio de Ciencia y Tecnología (Government of Spain) under the Grant No. MAT 2007-61609.

References

1. Padture, N. P., In situ-toughened silicon-carbide. *J. Am. Ceram. Soc.*, 1994, **77**(2), 519–523.
2. Kim, Y.-W., Mitomo, M. and Nishimura, T., Heat-resistant silicon carbide with aluminum nitride and erbium oxide. *J. Am. Ceram. Soc.*, 2001, **84**(9), 2060–2064.
3. Sigl, L. S., Thermal conductivity of liquid-phase-sintered silicon carbide. *J. Eur. Ceram. Soc.*, 2003, **23**(7), 1115–1122.
4. Ortiz, A. L., Muñoz-Bernabé, A., Borrero-López, O., Domínguez-Rodríguez, A., Guiberteau, F. and Padture, N. P., Effect of sintering atmosphere on the mechanical properties of liquid-phase-sintered SiC. *J. Eur. Ceram. Soc.*, 2004, **24**(10–11), 3245–3249.
5. Meléndez-Martínez, J. J., Castillo-Rodríguez, M., Domínguez-Rodríguez, A., Ortiz, A. L. and Guiberteau, F., Creep and microstructural evolution at high temperature of liquid-phase-sintered silicon carbide. *J. Am. Ceram. Soc.*, 2007, **90**(1), 163–169.
6. Borrero-López, O., Ortiz, A. L., Guiberteau, F. and Padture, N. P., Effect of liquid-phase content on the contact mechanical properties of liquid-phase-sintered α-SiC. *J. Eur. Ceram. Soc.*, 2007, **27**(6), 2521–2527.
7. Borrero-López, O., Ortiz, A. L., Guiberteau, F. and Padture, N. P., Microstructural design of sliding-wear-resistant liquid-phase-sintered SiC: an overview. *J. Eur. Ceram. Soc.*, 2007, **27**(11), 3351–3357.
8. Kim, Y.-W., Mitomo, M. and Nishimura, T., High-temperature strength of liquid-phase-sintered SiC with AlN and RE_2O_3 (RE = Y, Yb). *J. Am. Ceram. Soc.*, 2002, **85**(4), 1007–1009.
9. Nagano, T., Gu, H., Zhan, G.-D. and Mitomo, M., Effect of atmosphere on superplastic deformation behavior in nanocrystalline liquid-phase-sintered silicon carbide with Al_2O_3–Y_2O_3 additions. *J. Mater. Sci.*, 2002, **37**(20), 4419–4424.
10. Castillo-Rodríguez, M., Muñoz, A. and Domínguez-Rodríguez, A., Correlation between microstructure and creep behavior in liquid-phase-sintered α-silicon carbide. *J. Am. Ceram. Soc.*, 2006, **89**(3), 960–967.
11. Sánchez-González, J., Ortiz, A. L., Guiberteau, F. and Pascual-Centenera, C., Complex impedance spectroscopy study of a liquid-phase-sintered α-SiC. *J. Eur. Ceram. Soc.*, 2007, **27**(12–15), 3941–4395.
12. Can, A., McLachlan, D. S., Sauti, G. and Herrmann, M., Relationships between microstructure and electrical properties of liquid-phase-sintered silicon carbide materials using impedance spectroscopy. *J. Eur. Ceram. Soc.*, 2005, **27**(2–3), 1361–1363.
13. Volz, E., Roosen, A., Hartung, W. and Winnacker, A., Electrical and thermal conductivity of liquid phase sintered SiC. *J. Eur. Ceram. Soc.*, 2001, **21**(10–11), 2089–2093.

14. Maeda, M., Nakamura, K., Ohkubo, T. and Ishizuka, T., Oxidation behaviour of silicon carbide under cyclic and static conditions. *Ceram. Int.*, 1989, **15**(1), 1–6.
15. Gomez, E., Iturriza, I., Echeberria, J. and Castro, F., Oxidation resistance of SiC ceramics sintered in the solid state or in the presence of a liquid phase. *Scripta Mater.*, 1995, **33**(3), 491–496.
16. Liu, D.-M., Oxidation of polycrystalline α-silicon carbide ceramic. *Ceram. Int.*, 1997, **23**(5), 425–436.
17. Jensen, R. P., Luecke, W. E., Padture, N. P. and Wiederhorn, S. M., High-temperature properties of liquid-phase-sintered α-SiC. *Mater. Sci. Eng.*, 2000, **A282**(1–2), 109–114.
18. Rodríguez-Rojas, F., Borrero-López, O., Ortiz, A. L. and Guiberteau, F., Oxidation kinetics of pressureless liquid-phase-sintered α-SiC in ambient air at elevated temperatures. *J. Mater. Res.*, 2008, **23**(6), 1689–1700.
19. Singhal, S. C., Oxidation kinetics of hot-pressed silicon carbide. *J. Mater. Sci.*, 1976, **11**(7), 1246–1253.
20. Costello, J. A. and Tressler, R. E., Oxidation-kinetics of hot-pressed and sintered α-SiC. *J. Am. Ceram. Soc.*, 1981, **64**(6), 327–331.
21. Costello, J. A. and E: Tressler, R., Oxidation kinetics of silicon carbide crystals and ceramics: I. In dry oxygen. *J. Am. Ceram. Soc.*, 1986, **69**(9), 674–681.
22. Chartier, T., Laurent, J. M., Smith, D. S., Valdivieso, F., Goeuriot, P. and Thevenot, F., Oxidation resistance and electrical properties of silicon carbide added with Al_2O_3, AlN, Y_2O_3 and NiO. *J. Mater. Sci.*, 2001, **36**(15), 3793–3800.
23. Choi, H. J., Lee, J. G. and Kim, Y. W., Oxidation behavior of liquid-phase sintered silicon carbide with aluminum nitride and rare-earth oxides. *J. Am. Ceram. Soc.*, 2002, **85**(9), 2281–2286.
24. Biswas, K., Rixecker, G. and Aldinger, F., Improved high temperature properties of SiC-ceramics sintered with Lu_2O_3-containing additives. *J. Eur. Ceram. Soc.*, 2003, **23**(7), 1099–1104.
25. Guo, S., Hirosaki, N., Tanaka, H., Yamamoto, Y. and Nishimura, T., Oxidation behavior of liquid-phase sintered SiC with AlN and Er_2O_3 additives between 1200 °C and 1400 °C. *J. Eur. Ceram. Soc.*, 2003, **23**(12), 2023–2029.
26. Biswas, K., Rixecker, G. and Aldinger, F., Effect of rare-earth cation additions on the high temperature oxidation behavior of LPS–SiC. *Mater. Sci. Eng.*, 2004, **A374**(1–2), 56–63.
27. Suzuki, K., Kageyama, N. and Kanno, T., Improvement in the oxidation resistance of liquid-phase-sintered silicon carbide with aluminum oxide additions. *Ceram. Int.*, 2005, **31**(6), 879–882.
28. Weidenmann, K. A., Rixecker, G. and Aldinger, F., Liquid phase sintered silicon carbide (LPS–SiC) ceramics having remarkably high oxidation resistance in wet air. *J. Eur. Ceram. Soc.*, 2006, **26**(13), 2453–2457.
29. Singhal, S. C. and Lange, F. F., Effect of alumina content in the oxidation of hot-pressed SiC. *J. Am. Ceram. Soc.*, 1975, **58**(9–10), 433–435.
30. Ortiz, A. L., Bhatia, T., Padture, N. P. and Pezzotti, G., Microstructural evolution in liquid-phase-sintered SiC: Part III. Effect of nitrogen-gas sintering atmosphere. *J. Am. Ceram. Soc.*, 2002, **85**(7), 1835–1840.
31. Borrero-López, O., Ortiz, A. L., Guiberteau, F. and Padture, N. P., Effect of nature of intergranular phase on sliding-wear resistance of liquid-phase-sintered α-SiC. *Scripta Mater.*, 2007, **57**(6), 505–508.
32. Castillo-Rodríguez, M., Muñoz, A. and Domínguez-Rodríguez, A., Effect of atmosphere and sintering time on the microstructure and mechanical properties at high temperatures of α-SiC sintered with liquid phase Y_2O_3–Al_2O_3. *J. Eur. Ceram. Soc.*, 2006, **26**(12), 2397–2405.
33. Borrero-López, O., Pajares, A., Ortiz, A. L. and Guiberteau, F., Hardness degradation in liquid-phase-sintered SiC with prolonged sintering. *J. Eur. Ceram. Soc.*, 2007, **27**(11), 3359–3364.
34. Xu, H., Bhatia, T., Deshpande, S. A., Padture, N. P., Ortiz, A. L. and Cumbrera, F. L., Microstructural evolution in liquid-phase-sintered SiC: Part I, effect of starting powder. *J. Am. Ceram. Soc.*, 2001, **84**(7), 1578–1584.
35. Goldstein, J. I., Newbury, D. E., Echlin, P., Joy, D. C., Romig Jr., A. D., Lyman, C. E. *et al.*, *Scanning Electron Microscopy and X-Ray Microanalysis*. Plenum Press, New York, 1992.
36. Tanaka, H. and Zhou, Y., Low temperature sintering and elongated grain growth of 6H–SiC powder with AlB_2 and C additives. *J. Mater. Res.*, 1999, **14**(2), 518–522.
37. Tanaka, H., Hirosaki, N., Nishimura, T., Shin, D.-W. and Park, S.-S., Nonequiaxial grain growth and polytype transformation of sintered α-silicon carbide and β-silicon carbide. *J. Am. Ceram. Soc.*, 2003, **86**(12), 2222–2224.
38. Sánchez-Bajo, F., Ortiz, A. L. and Cumbrera, F. L., Analytical formulation of the variance method of line-broadening analysis for Voigtian X-Ray diffraction peaks. *J. Appl. Cryst.*, 2006, **39**(4), 598–600.
39. Nickel, K. G., Corrosion of advanced ceramics. Measurement and modelling. In *NATO ASI Series, Series E (Applied Sciences)*, *vol. 267*, 1994.
40. Nordberg, L. O., Nygren, M., Käll, P. O. and Shen, Z. J., Stability and oxidation properties of RE-α-sialon ceramics (RE = Y, Nd, Sm, Yb). *J. Am. Ceram. Soc.*, 1998, **81**(6), 1461–1470.
41. Nordberg, L. O., Käll, P. O. and Nygren, M., A mathematical analysis of the non-parabolic oxidation behavior of α-sialon matrices and composites. *Key Eng. Mater.*, 1995, **113**(39–48).
42. Persson, J. and Nygren, M., The oxidation-kinetics of β-sialon ceramics. *J. Eur. Ceram. Soc.*, 1994, **13**(5), 467–484.
43. Persson, J., Käll, P. O. and Nygren, M., Parabolic–nonparabolic oxidation-kinetics of Si_3N_4. *J. Eur. Ceram. Soc.*, 1993, **12**(3), 177–184.
44. Persson, J., Ekstrom, T., Käll, P. O. and Nygren, M., Oxidation behavior and mechanical-properties of β-sialons and mixed α-β-sialons sintered with additions of Y_2O_3 and Nd_2O_3. *J. Eur. Ceram. Soc.*, 1993, **11**(4), 363–373.
45. Lamkin, M. I., Riley, F. L. and Fordham, R. J., Oxygen mobility in silicon dioxide and silicate glasses: a review. *J. Eur. Ceram. Soc.*, 1992, **10**(5), 347–367.
46. Matusch, D., Phase Studies in the System Y–Si–Al–O–N, Ph.D. Thesis. University of Stuttgart, 2003.
47. Kolitsch, U., Seifert, H. J., Ludwig, T. and Aldinger, F., Phase equilibria and crystal chemistry in the Y_2O_3–Al_2O_3–SiO_2 system. *J. Mater. Res.*, 1999, **14**(2), 447–455.